Backward resonance production in $\pi^- p \to n\pi^+\pi^-$ at 8 GeV/c

B. Eisenstein, J. Elliott, W. Mollet,* B. Nelson,† D. S. Rhines,‡ R. G. Wagner,§ and W. T. Wroblicka
University of Illinois at Urbana-Champaign, Urbana, Illinois 61801

J. Watson
Argonne National Laboratory, Argonne, Illinois 60439

N. M. Gelfand¶ and G. R. Morris‖
University of Chicago, Chicago, Illinois 60637

(Received 27 December 1977)

We have studied backward meson and baryon production in $\pi^- p \to n\pi^+\pi^-$ at 8 GeV/c using a streamer chamber triggered by the detection of the interaction of the neutron in thick-plate optical spark chambers. Our data sample of 866 events is dominated by the quasi-two-body final states $\Delta^-(1232)\pi^+$, $n\rho^0$, and nf^0. We study the differential and total backward cross sections for these states and the decay angular distributions of the resonances. The results for the Δ^- and ρ^0 indicate that both nucleon and Δ exchange in the u channel are important in their production, while f^0 production is, as expected, consistent with nucleon exchange.

I. INTRODUCTION

As part of a study of backward meson and baryon production in 8-GeV/c $\pi^- p$ interactions we report here on the reaction

$$\pi^- p \to n\pi^+\pi^-. \tag{1}$$

Previous results have been published on the reaction

$$\pi^- p \to p\pi^+\pi^-\pi^- \tag{2}$$

at 8 GeV/c (Ref. 1) which showed the production of ρ^0, f^0, and baryon resonances in backward reactions. Backward resonance production has also been seen at 9 and 12 GeV/c in experiments which triggered on fast forward protons.[2]

The present experiment uses a fast forward neutron as the signature for baryon exchange. A liquid-hydrogen target inside the University of Illinois–Argonne National Laboratory streamer chamber was exposed to an 8-GeV/c π^- beam from the Argonne ZGS. The experimental trigger required the detection of a neutron interaction in thick-plate optical spark chambers downstream of the target within a time-of-flight window which eliminated slow neutrons, and yielded events of the type

$$\pi^- p \to nX^0. \tag{3}$$

Events with two, four, or six outgoing charged-particle tracks in the streamer chamber, plus a visible neutral-particle interaction in the spark chambers, were measured and fitted to track mass hypotheses of the form $\pi^- p \to n +$ (all charged). Measurement of the neutron's direction permitted three-constraint fits. The streamer chamber is especially suited for this experiment, since it combines time resolution with good multiple-track detection efficiency and large solid-angle acceptance.

Events with four or more final-state particles will be described in a future publication. Here we report on 866 events fitting reaction (1) and satisfying various selection criteria. We present evidence for the backward production of ρ^0, f^0, and $\Delta^-(1232)$, and discuss differential cross sections, decay angular distributions, and their implications for production mechanisms.

II. DATA ACQUISITION

The design of the experiment to study the reaction $\pi^- p \to nX^0$ was motivated by the goals of enhancing the baryon exchange signal relative to that of the normally dominant forward reactions and of obtaining kinematic information on all charged particles in the final state. These criteria were met by triggering on the interaction of a fast forward neutron in optical spark chambers, which also permitted a measurement of the direction of the neutron, and detecting the charged particles in the final state in a streamer chamber.

An elevation view schematic of the experimental layout is shown in Fig. 1. The π^- beam, streamer-chamber system, and liquid-hydrogen (LH_2) target are essentially identical to the apparatus used in the study of reaction (2) and previously described.[1,3,4] The 1.5-m × 1.0-m × 0.6-m streamer chamber contains a 30.5-cm × 3.8-cm-diameter hydrogen-target flask in a polyvinylchloride vacuum box.[3] A 14.5-kG horizontal magnetic field deflects beam particles upward. The events are photographed in 18° stereo by three cameras,

yielding records of outgoing tracks as well as ~20 cm of incident beam track upstream of the target. Since the beam track could not usually be reconstructed with adequate precision, additional information on the direction of the incident beam was provided by the three pairs of multiwire proportional chambers (MWPC's) upstream of the streamer chamber.

Scintillation counter B_4 was positioned over the hole in counter A_1 so that a beam particle passing through both the hole and B_4 traversed the entire target flask. The upstream pair of counters B_3 and A_0 served a similar function. Noninteracting beam particles leaving the region of magnetic field surrounding the streamer chamber passed through the array of counters labeled D. Thus, in addition to signals from some counters further upstream in the π^- beam, the logical signal for an interaction in the target required signals from B_3 and B_4, and no signals from A_0, A_1, or D.

Neutrons produced in target interactions were detected by their interaction in a system of spark chambers and scintillation counters beginning ~11 m from the target. The three spark chambers contained a total of 9 aluminum and 54 stainless steel plates with horizontal and vertical dimensions of 121.9 cm and 91.4 cm, respectively. The apparent location on film of the neutron interaction vertex for events in which the neutron interacted in the first or last plate of a chamber may be ambiguous with events in which the neutron interacted between chambers. This is especially true when the interaction produces only one visible charged secondary track. To reduce the number of such interactions, aluminum was used for the first two plates and the last plate of chamber 1, the first and last plate of chamber 2, and the first plate and last three plates of chamber 3. From the known absorption length values for iron and aluminum, and plate thicknesses of 0.305 cm for the steel and 0.318 cm for the aluminum, we find that the spark chambers contain a total of 1.0 nuclear absorption length of material. These chambers nominally accept neutrons produced at angles up to ~3° in the laboratory, corresponding to center-of-mass angles of ~165° to 180° for neutrons from $n\rho^0$ or nf^0 final states. In fact there is a nonzero acceptance at larger laboratory angles due to the dispersion of the beam and the fact that neutrons produced at 0° with respect to the average beam direction passed through the most upstream spark chamber slightly above center.

The "neutron signal" was formed by the detection of charged secondaries from a neutron interaction in planes of scintillation counters, labeled N in Fig. 1, located immediately downstream of each chamber. Each plane contained four counters of dimensions 91.5 cm × 35.6 cm × 0.95 cm with photomultiplier tubes attached to both ends of each counter. The counters were overlapped by a few centimeters and together they covered the active area of each spark chamber. A neutron time-of-flight selection was imposed on the signal to eliminate low momentum neutrons and background. This cut required the neutron signal to fall within a time gate set relative to a signal of the entrance of an incident π^- into the target. It was necessary to require a signal from at least two of the three planes of scintillator in order to achieve a neutron signal relatively free from background.

The spark chambers were photographed in 90° stereo from the top and side. All six views were recorded by a single camera through the use of a system of mirrors. This method of detection allowed reconstruction of the neutron vertex in space to within ±1.5 cm. For neutrons of interest, whose momenta ranged from ~2 to ~8 GeV/c, the total spread in flight time at 11 m is ~3.5 nsec. No attempt was made to resolve the neutron time of flight and thereby measure the momentum.

Most of the background of photons and charged particles incident on the spark chambers was vetoed by a lead plate and scintillation counter hodoscope positioned ~8.5 m downstream of the tar-

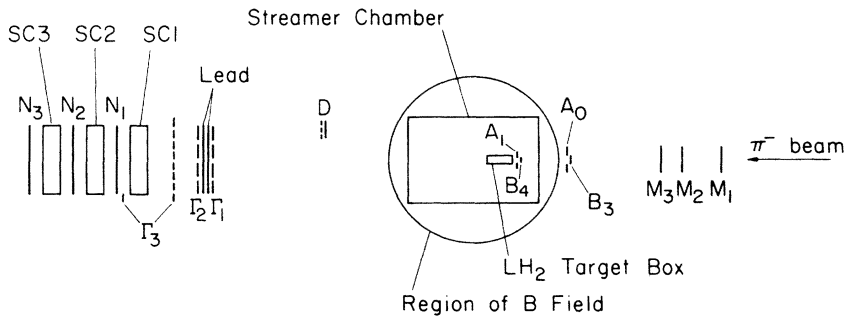

FIG. 1. Elevation view of experimental layout (not to scale). $M_{1,2,3}$ denote multiwire proportional chambers. $A_{0,1}$ and $B_{3,4}$ are scintillation counters. D, $\Gamma_{1,2,3}$, $N_{1,2,3}$ denote scintillation hodoscopes. $SC_{1,2,3}$ are spark chambers.

get. This "γ filter" was composed of 5.1 radiation lengths of lead sandwiched between two 101-cm-high by 137-cm-wide planes of scintillator, labeled $\Gamma_{1,2}$ in Fig. 1. A third 152-cm-high by 178-cm-wide plane of counters, Γ_3, associated with the γ filter, was located just upstream of the first spark chamber and 10.5 m from the target. Additional veto counters were placed below the first spark chamber to reduce triggers by secondaries from interactions in the chamber stands.

A "filtered" neutron signal was formed by a count from any of the twelve neutron counters associated with the spark chambers in anticoincidence with the γ filter logic. To reduce triggering on tube noise, a neutron counter signal required coincident counts from both the upper and lower phototubes. Signals from each plane were sent to the two-out-of-three plane majority logic and the "master coincidence" for the experimental trigger was then formed by the signal of a π^- interaction in the LH_2 target in coincidence with both a filtered neutron signal falling inside the time-of-flight gate and a two-out-of-three neutron majority-logic pulse.

The minimum width of the time-of-flight window necessary to accept backward neutrons of interest was estimated to be ~8 nsec. This represents the sum of the ~3.5 nsec spread in neutron arrival times and ~4.5 nsec which includes the finite size of the neutron counters, timing jitter in the electronics, and timing errors. Background triggers were studied by measuring the relative trigger rate as a function of the relative time delay between the filtered neutron signal and an 8-nsec time gate (Fig. 2). From Fig. 2 it can be seen that the amount of signal outside the prompt peak is small. This allowed the time gate for experimental running to be set to 23 nsec which avoided any possibility of timing too tightly yet did not introduce a significantly higher background trigger rate.

The fraction of triggers due to photons was studied by measuring the master coincidence rate as a function of the lead thickness in the γ filter. We find that in the absence of lead the photon to neutral hadron trigger ratio is 10.8/1, while for the 2.8 cm of lead used during normal running the ratio is 1/4.2. Thus the lead reduces the photon trigger rate by 98%, while the combination of lead and scintillator reduce the neutral hadron rate by only 20%. We note here that this rate includes triggers from K_L^0's as well as neutrons.

The data on reaction (3) were obtained in two experimental runs.[5,6] Between these runs several improvements on the apparatus were made to reduce backgrounds. As a measure of improvement we note that the target-full and -empty trigger

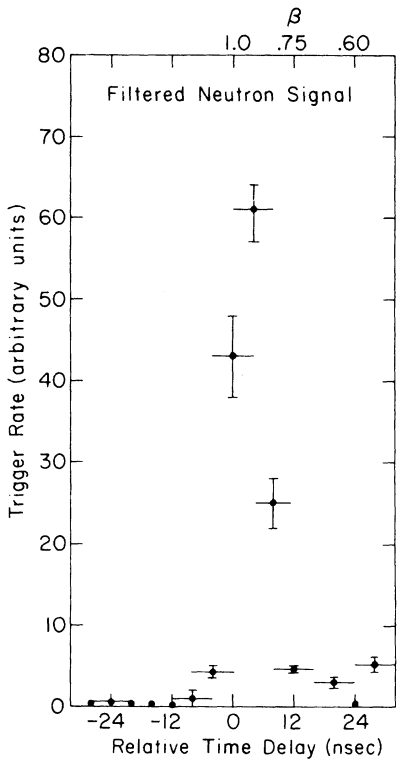

FIG. 2. The relative trigger rate vs the relative time delay between the filtered neutron signal and an 8-nsec-wide time gate. The origin is chosen so that zero delay corresponds to particles with $\beta=1$. Counts at negative delay ($\beta>1$) are due to accidental coincidences.

rates of the first run, 24.0 and 8.4 per 10^5 incident π^-, became 18.0 and 4.4 per 10^5 π^- in the second.

Many conditions were common to both runs. With a streamer-chamber memory time of ~3 μsec and a 600-msec ZGS spill width, the beam intensity was maintained at ~18 000 targeted π^-'s per ZGS pulse to inhibit the presence of extra beam tracks in streamer chamber pictures. A picture-taking rate of 1.5–2.0 per spill was achieved with the maximum of 3 per pulse being determined by the 200-msec experimental dead time necessary for recharging the streamer-chamber high-voltage system.

The numbers of pictures taken during the initial and final runs with the $\pi^- p \to nX^0$ trigger were 180 000 and 240 000, respectively. During the final run there were also 8 000 pictures taken with an interacting beam trigger and no neutron or γ filter requirement, and 18 500 pictures taken triggering on $pp \to nX^{++}$. These two sets of data were used to check the cross-section normalization which is discussed in Appendix B. In both runs noninteracting beam tracks were periodically photographed. In addition to their use for the determination of

the average momentum and lab angles of the beam, the tracks served to locate the MWPC's with respect to the streamer-chamber coordinate system.

The average beam momentum was determined to be 7.93 GeV/c for the first run and 8.04 GeV/c for the final run. The beam momentum bites for the first and second run were set to ±1.7% and ±2.9%, respectively.

III. DATA REDUCTION

The 420 000 streamer-chamber picture triads were double scanned for events with two, four, or six outgoing tracks with net charge zero, as well as vees and noninteracting beam tracks. 76% (19%) as many four- (six-) prong as two-prong events were found. Events were considered measurable if all tracks and fiducial marks were visible in at least two views.

For each measurable event of interest the corresponding spark-chamber frame was scanned for a neutral interaction. The event was selected for further analysis if it had a neutral interaction vertex (up to 3 if ambiguities existed). 11% of the neutral interactions were unambiguously identified as electromagnetic showers. These events were processed as if they were neutron candidates and were found to make a negligible contribution to the final data sample.

The streamer and spark chamber film was measured on DOLLY,[7] the University of Illinois semiautomatic measuring machine. The streamer-chamber track measurements were processed as described in Ref. 1 through TVGP and VERTEX, which was needed to extrapolate the tracks to the production vertex which is obscured by the target box. Separate programs reconstructed the neutron interaction vertex in space and determined the direction of the incident beam using, when available, MWPC and streamer-chamber information. When the MWPC data was insufficient, averaged values of the beam angles were used. The averaged value of the beam momentum was always assumed.

SQUAW was used to fit the measurements to reaction (1) and several other mass hypotheses. These others included elastic scattering, K_L^0 triggers, additional π^0 or missing mass, etc. A fit was tried for each possible neutral interaction vertex determined for the event. All constrained fits with $\chi^2 \leq 60$, and unconstrained (0C) "fits" with physical solutions were kept for later consideration. We note that the fit to reaction (1), lacking only the magnitude of the neutron momentum, is 3C.

From the entire film sample, 54 550 two-prong events with a neutron interaction vertex in the spark chambers were successfully measured, reconstructed, and had a primary vertex determined. The missing-mass-squared distribution for these events, shown in Fig. 3, exhibits a signal for a single missing neutron at the edge of a large background of events with additional missing neutral particles. In all, 1 663 events had a fit to reaction (1) with a $\chi^2 \leq 60$.

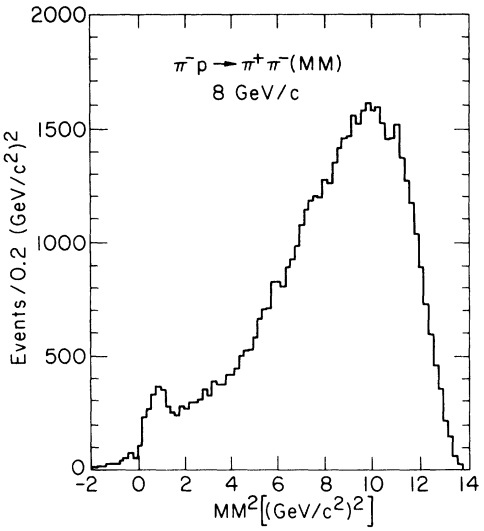

FIG. 3. The missing-mass-squared distribution for two-prong events successfully processed by VERTEX, calculated assuming that the outgoing charged particles are pions.

For the sample of 1 663 events the distribution in $\cos\theta^*_{pn}$, where θ^*_{pn} is the scattering angle between incident and outgoing nucleons in the overall c.m., shows a large peak at $\theta^*_{pn} = 180°$ and a small one at $\theta^*_{pn} = 0°$. By requiring that the fitted neutron momenta, whose distribution is shown in Fig. 4, exceed 2 GeV/c, all 306 forward hemisphere events are removed from the sample, while the backward events are unaffected. An additional 348 events were removed from the sample by a target fiducial-volume cut, a requirement that each measured track was well fitted in TVGP by a space curve, and that the tracks extrapolated to a common vertex within a specified tolerance. These selection criteria were intended to eliminate events with poorly measured tracks or in which outgoing tracks scattered or decayed within the target box. The ensuing loss of real events was estimated and included in the cross-section calculation of Appendix B.

The kinematic χ^2 for the remaining 1 009 events is shown in Fig. 5. The solid curve is a fit to the data incorporating a constant term in addition to the expected 3C χ^2 distribution. There are some events for which we do not reliably estimate cor-

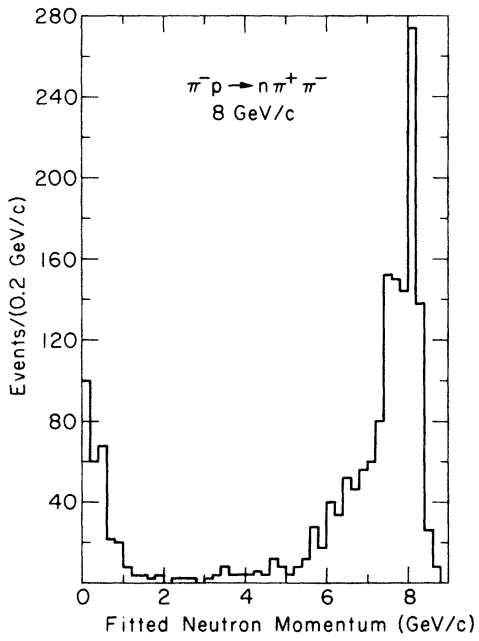

FIG. 4. The distribution of fitted neutron momentum for 1 663 events which fit $\pi^- p \to n\pi^+\pi^-$.

rections to the track parameter errors in the vertex extrapolation procedure, and so we believe that many of the events in the "tail" in Fig. 5 ($\chi^2 \gtrsim 20$) are real. A study of the signal for $\Delta^-(1232)$ in the $n\pi^-$ invariant mass combination, which will be seen in Sec. IV A to be sharp and relatively free of background, motivated the choice of $\chi^2 \leq 40$ for the final event selection. We estimate that only ~6% of real $n\pi^+\pi^-$ events have $\chi^2 > 40$ and that only 23% of the fits with $\chi^2 \leq 40$ can be background.

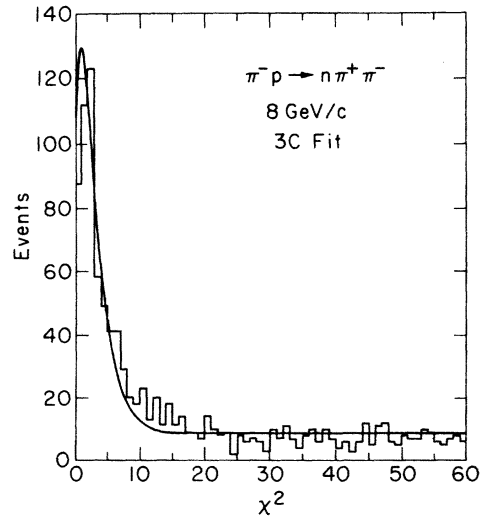

FIG. 5. The kinematic χ^2 distribution for 1 009 events satisfying the selection criteria described in the text. The solid curve is a fit to a constant plus a χ^2 distribution with three degrees of freedom.

After the χ^2 selection, 866 events remain. These events were carefully studied to determine whether they were contaminated by possible mass misidentification with other 3C hypotheses and it was concluded that such problems existed at a level of ~5% at most. This is not surprising since the charged tracks typically have momenta less than 1 GeV/c. The major source, then, of background contamination is events with the final state $n\pi^+\pi^-\pi^0$.

In the following analysis of the $n\pi^+\pi^-$ final state it is necessary to weight the events to correct for the geometrical acceptance of the streamer and spark chambers. The method of weight calculation is described in Appendix A. The average weight of observed events was studied as a function of $\cos\theta^*_{pn}$ and of $M(\pi^+\pi^-)$. The average weight varied only by $\sim \pm 20\%$ over the entire range of observed $\pi^+\pi^-$ mass. On the other hand, although it varied smoothly from a value of 2 at $\cos\theta^*_{pn} = -1$ to 6 at $\cos\theta^*_{pn} = -0.96$, the average weight increased very rapidly for $\cos\theta^*_{pn} > -0.96$. This is a direct consequence of the finite solid angle subtended by the spark chambers. For this reason the analysis of the features of the $\pi^+\pi^-$ system was performed using a restricted angular region.

The average weights for observed events as functions of the $n\pi^\pm$ invariant mass were constant to within $\sim \pm 40\%$. However, the direction in the laboratory of the decay neutron from a baryon resonance is sensitive to the form of the decay angular distribution. This problem will be addressed in the discussion of the $\Delta^-(1232)\pi^+$ final state in Sec. IV A.

IV. DATA ANALYSIS

A. The $(n\pi^+)\pi^-$ and $(n\pi^-)\pi^+$ final states

In Fig. 6 are shown the $n\pi^+$ and $n\pi^-$ invariant-mass distributions for the 866-event sample, along with diagrams indicating the allowed isospins for baryon exchange. The only prominent feature is the production of $\Delta^-(1232)$ over a small background estimated to be $(9 \pm 2.5)\%$. An examination of the Dalitz plot for the $n\pi^+\pi^-$ final state shows that the peaking at large $n\pi^+$ mass reflects the production of Δ^- as well as ρ^0 and f^0 in $\pi^+\pi^-$.

Because of the absence of any signal for $\Delta^+(1232)$ decaying to $n\pi^+$ the data appear consistent with the hypothesis that nucleon exchange ($I = \frac{1}{2}$) is dominant over Δ exchange ($I = \frac{3}{2}$) in the u channel. However, a large contribution from Δ exchange cannot be ruled out. To illustrate this we write the matrix elements M_+ and M_- for Δ^+ and Δ^- production as

$$M_+ = (\tfrac{2}{5})^{1/2} A_3^u ,$$

$$M_- = (\tfrac{2}{15})^{1/2} A_3^u + (\tfrac{1}{3})^{1/2} A_1^u ,$$

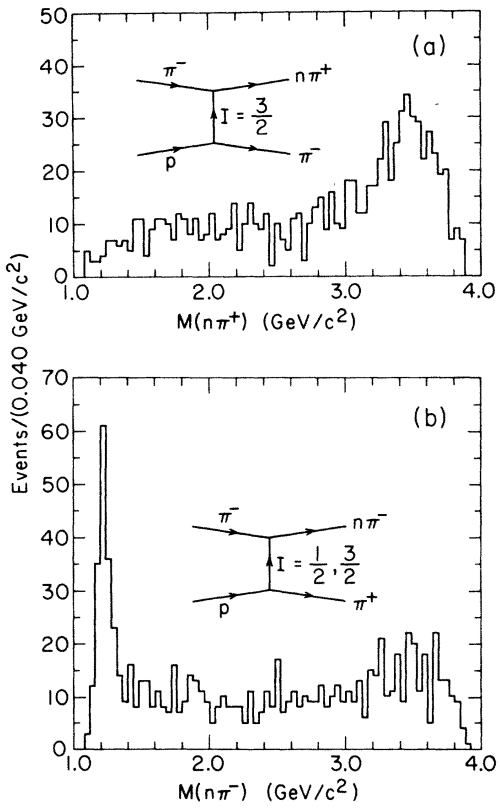

FIG. 6. The $n\pi$ invariant-mass distributions for the final sample of 866 events. The permitted isotopic-spin exchanges are also shown: (a) $M(n\pi^+)$, (b) $M(n\pi^-)$.

where A_3^u and A_1^u are the u-channel amplitudes for $I=\frac{3}{2}$ and $I=\frac{1}{2}$ exchange, respectively. We approximate the ratio of the production of Δ^+ to Δ^- by the square of the magnitude of these matrix elements, and relate that to the ratio of observed events, r, by including the branching ratio of $\frac{1}{3}$ for $\Delta^+ \to n\pi^+$. If we set $A_3^u/A_1^u = \alpha e^{i\phi}$, the magnitude α may be found for any assumption about the phase ϕ. The maximum possible value of α results from the assumption that $\phi = 0°$.

We observe a $\Delta^-(1232)$ signal of 157 events with mass <1.33 GeV/c^2 above a background of 16 events (estimated). If we assume the same number of background events for $M(n\pi^+)<1.33$ GeV/c^2, we arrive at a possible Δ^+ signal of 14 events and the value $r=0.09$. From this we find $\alpha=0.67$ ($\phi=0°$). A less plausible assumption would be that all $n\pi^+$ events with $M<1.33$ GeV/c^2 could be attributed to Δ^+ decay, leading to a maximum α of 1.13. Clearly, the absence of observed Δ^+ production does not exclude the possibility that $I=\frac{3}{2}$ exchange contributes with a strength comparable to $I=\frac{1}{2}$ exchange. Rougé *et al.*[2] report a similar upper limit on $\alpha(0.98)$ in the study of the backward reaction $\pi^- p \to p\pi^-\pi^0$ at 9GeV/c.

As was suggested in Sec. III, the finite size of the neutron chambers limits the acceptance for neutrons from the decay of a $\Delta^-(1232)$. The decay of a spin-$\frac{3}{2}$ baryon into $n\pi^-$ is described by the density matrix $\rho_{2m,2m'}$ with the normalization $\rho_{11}+\rho_{33}=\frac{1}{2}$. The decay angles of the neutron, θ^D and ϕ^D, are specified in the Gottfried-Jackson frame whose z axis is in the direction of the incident beam and whose y axis is normal to the production plane.[8] In order to compare the observed events with $M(n\pi^-)<1.33$ GeV/c^2 to various hypotheses for the values of the density matrix elements, Monte Carlo event samples were generated and processed through the same experimental detection routines as were used to calculate event weights. The events were generated according to $dN/du' \propto e^{-bu'}$, where $u'=u_{\max}-u$ and u is the four-momentum transfer from the beam to the Δ^-. The resulting distributions in u', $\cos\theta^D$, and ϕ^D were compared to the observed events. It was found that no Monte Carlo distributions were sensitive to the assumed values for $\mathrm{Re}\rho_{3,1}$ or $\mathrm{Re}\rho_{3,-1}$ so these were set equal to zero. Only ρ_{11} (or ρ_{33}) then remains as a density matrix element that can be varied.

Figure 7 shows the detection efficiency as a function of u' for events generated with $\rho_{11}=0.18$, but the efficiency is insensitive to the assumed value. In the event generation it is assumed that the density matrix elements are independent of u'. This assumption cannot hold at $u'=0$ since ρ_{33} must vanish there as a consequence of angular momentum conservation, but from the preceding observation this has no significant effect on the u' detection efficiency.

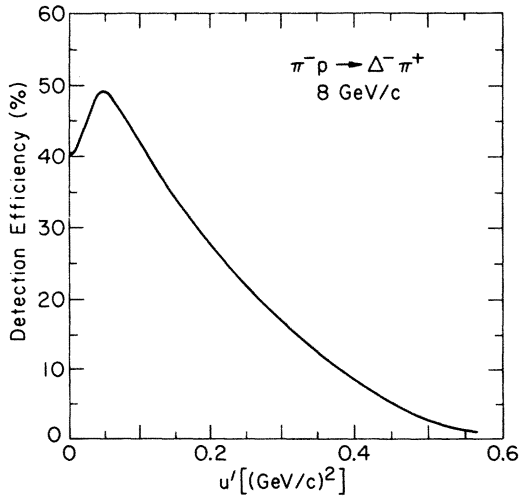

FIG. 7. The detection efficiency for events of the type $\pi^- p \to \Delta^-(1232)\pi^+$, calculated as a function of u' using the Monte Carlo described in the text. A value of $\rho_{11}=0.18$ has been assumed.

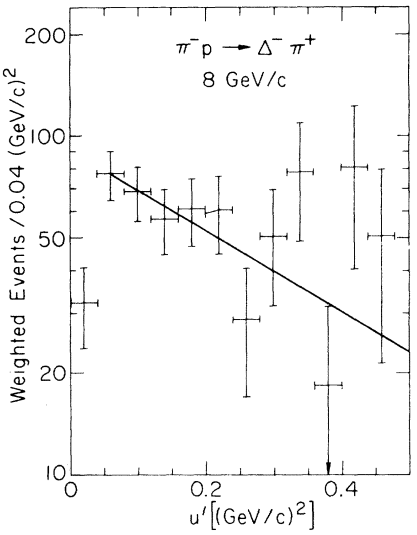

FIG. 8. The distribution of u' to the $\Delta^-(1232)$, corrected for the detection efficiency shown in Fig. 7. The solid line is the result of the fit described in the text and whose parameters appear in Table I.

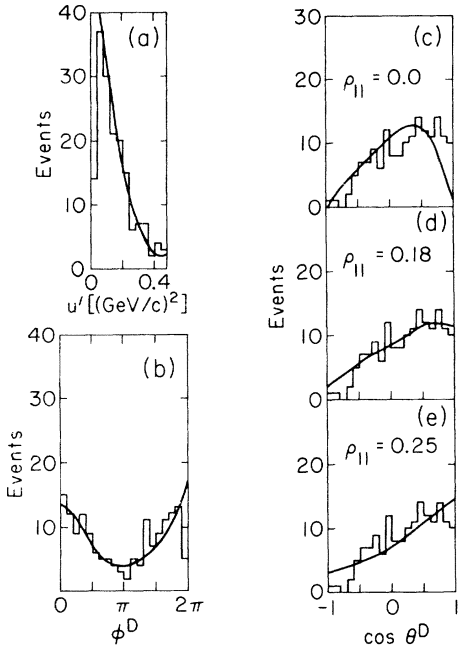

FIG. 9. The observed distributions of u', $\cos\theta^D$, and ϕ^D for the $\Delta^-(1232)$. The curves show the distributions for events generated by the Monte Carlo described in the text and subjected to the experimental acceptance. Except as noted, ρ_{11} was fixed at 0.18: (a) u', (b) ϕ^D, (c) $\cos\theta^D$ for $\rho_{11}=0.0$, (d) $\cos\theta^D$, (e) $\cos\theta^D$ for $\rho_{11}=0.25$.

The experimental u' distribution for Δ^- events, corrected using the detection-efficiency curve of Fig. 7, is shown in Fig. 8. A striking feature is the sharp decrease in the differential cross section for $u'<0.04$ GeV/$c)^2$. This dip, which cannot be attributed to experimental acceptance, is similar to one seen near $u'=0$ for the reaction $\pi^- p \to \Delta^- \pi^+$ at lower incident beam momenta,[9] where possible explanations were suggested. The dip can occur in any model in which the helicity-flip amplitude is small compared to the nonflip amplitude. In particular, we assume that ρ_{33}, which must vanish for $u'=0$, is nonzero at $u' \gtrsim 0.04$ $(\mathrm{GeV}/c)^2$.

The data in the interval $0.04 \leq u' \leq 0.40$ $(\mathrm{GeV}/c)^2$ were fitted to the form $dN/du' = Ae^{-bu'}$. The resulting fit, shown in Fig. 8, yields the numbers shown in Table I. The cross section was determined by adding the number of events in the first bin to the integral of $Ae^{-bu'}$ from 0.04 $(\mathrm{GeV}/c)^2$ to ∞, and multiplying by the cross-section basis, σ_b, given in Appendix B. Also given is R, the ratio of the number of events with $u'<0.04$ $(\mathrm{GeV}/c)^2$ to the number predicted by the extrapolation of $Ae^{-bu'}$ to $u'=0$. If one assumes that ρ_{11} does not vary with u', and that the dip is a consequence of the vanishing of ρ_{33}, then $R=2\rho_{11}$. This gives the value of $\rho_{11}=0.18$ and is consistent with $\rho_{11}=0.15$ found for $\pi^- p \to \Delta^0(1232)\pi^0$ at 9 GeV/c (Ref. 2). We emphasize that the value obtained for R is insensitive to the value of ρ_{11} assumed for the Monte Carlo calculation of the detection efficiency.

TABLE I. Values obtained from the fit of Δ^- events to the form $dN/du' = Ae^{-bu'}$. The value of σ was obtained using the cross-section normalization. The ratio R is defined in the text.

Quantity	Value
A	91.4 ± 16.5 events/0.04 $(\mathrm{GeV}/c)^2$
b	2.77 ± 1.12 $(\mathrm{GeV}/c)^{-2}$
σ	1.63 ± 0.79 μb
R	0.37 ± 0.12

The values $\rho_{11}=0.18$, $b=2.77$ were used to generate a sample of Monte Carlo events that were subjected to the experimental acceptance. The resulting distributions were scaled to the observed number of events and are shown in Fig. 9. We note excellent agreement with the u', $\cos\theta^D$, and ϕ^D distributions. The shapes of the u' and ϕ^D distributions are insensitive to the input parameters, being determined primarily by the experimental acceptance. Also shown in Fig. 9 are the $\cos\theta^D$ distributions generated for $\rho_{11}=0$ and $\rho_{11}=0.25$. The choice $\rho_{11}=0$ predicts too few events near $\cos\theta^D=1$ and is ruled out. Values of ρ_{11} larger than 0.25 predict too many events near $\cos\theta^D=1$ and are also excluded. If the production of Δ^- proceeded only by the exchange of a particle with

$J=\frac{1}{2}$, ρ_{11} would be 0.5, in clear contradiction to our results. Thus both $J=\frac{3}{2}$ (Δ) exchange and $J=\frac{1}{2}$ (nucleon) exchange must be present.

B. The $n(\pi^+\pi^-)$ final state

The $\pi^+\pi^-$ invariant-mass distribution for the final sample of 866 events is shown in Fig. 10 and displays enhancements corresponding to ρ^0 and f^0 production. The shaded distribution results from the removal of 167 events with $M(n\pi^-)<1.33$ GeV/c^2 and 9 events whose $\pi^+\pi^-$ mass was between 0.485 and 0.510 GeV/c^2, which were attributed to the reaction $\pi^- p \to \Lambda^0 K_S^0$. This interval is slightly larger than twice the experimental mass resolution of 9 MeV/c^2 in this region. The Δ^- events that were removed had a $\pi^+\pi^-$ mass distribution that was featureless and affected the remaining data primarily above 1 GeV/c^2. The solid line in Fig. 10 represents a fit to the shaded distribution of relativistic Breit-Wigner shapes for the ρ^0 and f^0 plus a smooth background that was constrained to be zero at the extreme allowed values of $M(\pi^+\pi^-)$. In the fit the widths of the ρ^0 and f^0 were fixed at 152 and 180 MeV/c^2, respectively. Only the data between 0.61 and 1.81 GeV/c^2 were used for the fit, the lower limit helping to reduce the effect of the excess of events on the low side of the ρ^0. The resulting masses were $M_{\rho^0}=729\pm12$ MeV/c^2 and $M_{f^0}=1249\pm10$ MeV/c^2. The ρ^0 mass is 30–40 MeV/c^2 below that typically seen in forward reactions and may reflect the dynamics of baryon exchange.

It is clear that there is an excess of events with $M(\pi^+\pi^-)\lesssim 0.7$ GeV/c^2 that is not satisfactorily explained by a Breit-Wigner form for the ρ^0 plus a smooth background. The possibility exists that some of the low mass events are examples of $n\pi^+\pi^-\pi^0$ events that had a 3C fit to reaction (1).

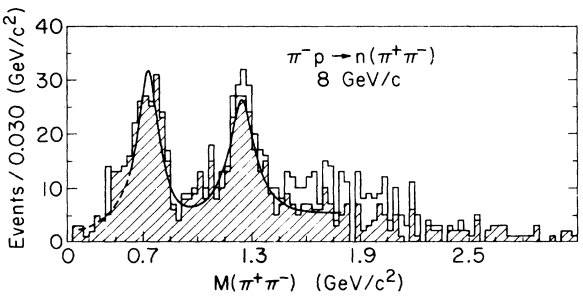

FIG. 10. The $\pi^+\pi^-$ invariant-mass distribution for 866 events. The shaded distribution results from the removal of 167 events with $M(n\pi^-)<1.33$ GeV/c^2 and 9 events which were attributed to the final state $K_S^0\Lambda^0$. The solid curve is a fit of the data from 0.61 GeV/c^2 to 1.81 GeVc^2 to two Breit-Wigner distributions plus a smooth background.

A study of the 0C solutions for the fitted events indicates the possibility of ~10 events being from the reaction $\pi^- p \to n\omega^0$. The $\pi^+\pi^-$ invariant masses from these candidates, however, are smoothly distributed from threshold to ~0.7 GeV/c^2, and cannot be responsible for the excess in question. Further studies of possible background contamination do not support the hypothesis that the excess is due to events incorrectly fitted to reaction (1).

The u' and decay angular distributions of the ρ^0 and f^0 events were studied by selecting events in the mass regions 0.64–0.85 GeV/c^2 and 1.15–1.33 GeV/c^2. In these regions estimates of the non-ρ^0 and non-f^0 backgrounds were taken from the fit to the mass spectrum and are ~15% in both cases. The restriction that $\cos\theta^*_{pn}\leq -0.96$, made to exclude events with poor detection efficiency as described in Sec. III, corresponded to selecting $u'<0.27$ (GeV/c)^2 for the ρ^0 and $u'<0.24$ (GeV/c)^2 for the f^0.

Figure 11 shows the acceptance-corrected u' distributions for the ρ^0 and f^0. A background subtraction has been made by subtracting the u' distribution for bins adjacent to each resonance, scaled by the number of background events given by the fit to the mass distribution. Neither the acceptance correction nor the background subtraction affected the character of either distribution. A fit to the form $d\sigma/du' = Ae^{-bu'}$ was performed for each, and in Table II are shown the fitted values for A, b, and the integrated cross section σ. We note that the errors on these numbers, as well as on the u' distributions, include the uncertainty in the cross-section normalization and the statistical

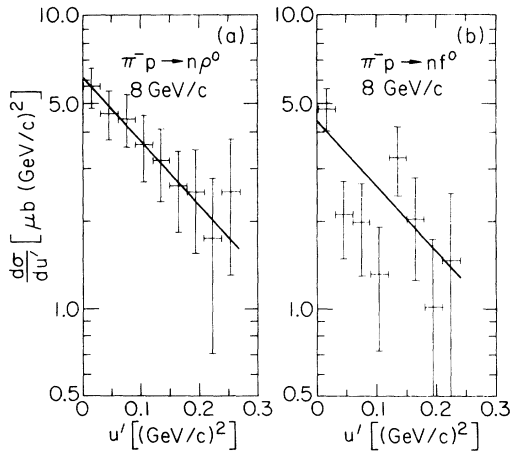

FIG. 11. The weighted distributions of u' to ρ^0 and f^0. A background subtraction, described in the text, has been performed in addition to the correction for experimental acceptance. The solid lines are the results of fits described in the text and whose parameters appear in Table II: (a) ρ^0 region (0.64–0.85 GeV/c^2), (b) f^0 region (1.15–1.33 GeV/c^2).

TABLE II. Values obtained from the fit of ρ^0 and f^0 events to the form $d\sigma/du' = Ae^{-bu'}$. The f^0 cross section refers only to the observed decay mode.

State	A [μb/(GeV/c)^2]	b [(GeV/c)$^{-2}$]	σ (μb)
$n\rho^0$	6.09 ± 1.20	4.94 ± 1.44	1.23 ± 0.43
nf^0	4.31 ± 0.93	5.12 ± 1.75	0.84 ± 0.34

error on the events in each bin. We see from Fig. 11 that $d\sigma/du'$ for the ρ^0 agrees well with a simple exponential, but that the f^0 displays a dip near $u' = 0.1$ (GeV/c)^2 or $u \sim -0.14$ (GeV/c)^2. We note that this is the approximate location of the dip predicted by a simple Regge-pole model in which the N_α trajectory is dominant.[10] Since the f^0 has $I = 0$, the only allowed exchange is $I = \frac{1}{2}$ and the dominance by N_α is a natural expectation.

Both $I = \frac{1}{2}$ and $I = \frac{3}{2}$ exchanges are allowed for the production of ρ^0. In the spirit of the estimate made for Δ^+ vs Δ^- production, we compare the reaction $\pi^- p \to n\rho^0$ with the published value of $\sigma(\pi^- p \to p\rho^-) = 1.86 \pm 0.2$ μb at 8 GeV/c (Ref. 11). Denoting the $I = \frac{3}{2}$ and $I = \frac{1}{2}$ amplitudes in this case by B_3^u and B_1^u, we find matrix elements

$$M_0 = (\tfrac{2}{9})^{1/2} B_3^u - (\tfrac{2}{9})^{1/2} B_1^u ,$$

$$M_- = B_3^u ,$$

for $n\rho^0$ and $p\rho^-$, respectively. Using Table II we find the ratio of ρ^- to ρ^0 cross sections to be 1.51 ± 0.55, and if we write $B_3^u/B_1^u = \beta e^{i\theta}$ we find extremes of $\beta \sim 0.37 \pm 0.03$ if $\theta = 0°$ and $\beta = 1.5^{+1.0}_{-0.5}$ if $\theta = 180°$.

The decay angular distributions for the ρ^0 and f^0, corrected for acceptance, are shown in Fig. 12 where θ^D and ϕ^D specify the direction of the π^+ in the Gottfried-Jackson frame whose z axis is in the direction of the target proton and whose y axis is normal to the production plane. The decay of an object of definite J^P produces a ϕ^D distribution that exhibits fourfold symmetry about $\pi/2$, π, and $3\pi/2$. This does not obtain in the case of ρ^0 and it is necessary to introduce an s-wave $\pi^+\pi^-$ background that interferes with the ρ^0 in order to fit the ϕ^D distribution. The possibility that the depletion of events near $\phi^D = \pi$ was due to some experimental detection inefficiency was exhaustively studied and ruled out.

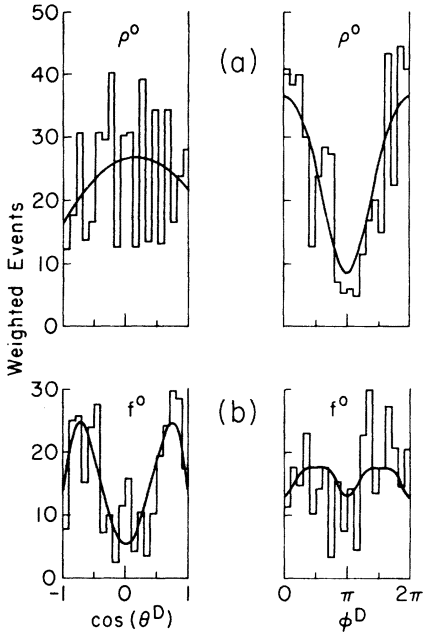

FIG. 12. The weighted decay angular distributions for ρ^0, (a), and f^0, (b), events. The solid curves display the distributions calculated from the density matrix elements given in Table III and the functional forms described in the text.

The decay angular distribution resulting from an interference between 1^- and 0^+ initial states has the form

$$W(\theta^D, \phi^D) = \frac{1}{4\pi}\left[1 + (\rho_{00} - \rho_{11})(3\cos^2\theta^D - 1) - 3\rho_{1-1}\sin^2\theta^D \cos 2\phi^D - 6\sqrt{2}\,\mathrm{Re}\rho_{10}\cos\theta^D \sin\theta^D \cos\phi^D \right.$$

$$\left. + 2\sqrt{3}\,\mathrm{Re}\rho_{0s}\cos\theta^D - 2\sqrt{6}\,\mathrm{Re}\rho_{1s}\sin\theta^D\cos\phi^D\right] ,$$

where the subscripts 0, ± 1 refer to the spin-1 state and the subscript s to the state with spin 0. Only the trace condition, $2\rho_{11} + \rho_{00} + \rho_{ss} = 1$, has been imposed. The density matrix elements were calculated using a moment analysis of the decay angular distributions, and are listed in Table IV. The table also presents the density matrix elements for the f^0, in which case a pure spin-2 state was assumed. The solid curves in Fig. 12 give the shape of the $\cos\theta^D$ and ϕ^D projections of the decay angular distributions from the calculated values of Table III.

In the case of the ρ^0, we see that the helicity-1 and -0 states are almost equally probable. The only off-diagonal density matrix element that is significantly different from zero is $\mathrm{Re}\rho_{1s}$. Although ρ_{11}, ρ_{00}, and ρ_{ss} cannot separately be determined we may ask if our results are internally consist-

TABLE III. Density matrix elements for the ρ^0 and f^0.

Resonance	Density matrix element	Value
ρ^0	$\rho_{00}-\rho_{11}$	-0.11 ± 0.05
	$\rho_{1,-1}$	0.03 ± 0.03
	$\mathrm{Re}\rho_{10}$	0.01 ± 0.02
	$\mathrm{Re}\rho_{0s}$	0.03 ± 0.02
	$\mathrm{Re}\rho_{1s}$	-0.15 ± 0.01
f^0	ρ_{22}	0.05 ± 0.03
	ρ_{11}	0.39 ± 0.02
	ρ_{00}	0.13 ± 0.04
	$\rho_{2,-2}$	-0.03 ± 0.02
	$\rho_{1,-1}$	0.08 ± 0.04
	$\mathrm{Re}\rho_{21}$	0.02 ± 0.02
	$\mathrm{Re}\rho_{20}$	-0.01 ± 0.02
	$\mathrm{Re}\rho_{2,-1}$	0.06 ± 0.03
	$\mathrm{Re}\rho_{10}$	-0.02 ± 0.03

ent. The density matrix element ρ_{1s} is constrained by $|\rho_{1s}| \leq (\rho_{11}\rho_{ss})^{1/2}$. With $\mathrm{Re}\rho_{1s}=-0.15$ we find that it is possible to satisfy the constraint, and also the trace condition, for a range of possible values for ρ_{11} and ρ_{ss}. These include ρ_{ss} values of 0.1 to 0.2 which are suggested by the estimate of ~15% background under the ρ^0 in the fit to the mass distribution.

The ρ_{2m} density matrix elements for the f^0 are all consistent with zero. This supports a model in which the production is dominated by $J=\frac{1}{2}$ (nucleon) exchange. Furthermore, the other off-diagonal density matrix elements are also very small. The helicity-1 state dominates, in contrast to the ρ^0 where helicty 0 and 1 are almost equally probable.

C. Summary and remarks

The reaction $\pi^- p \to n\pi^+\pi^-$ has been studied in the kinematic region where baryon exchange is expected to be the dominant production mechanism. The final state is dominated by $\Delta^-(1232)$, ρ^0, and f^0 production as it is in forward (meson exchange) reactions.

Although the absence of any clear signal for $\Delta^+(1232)$ production suggests that the $I=\frac{3}{2}$ exchange amplitude may be small compared to the $I=\frac{1}{2}$ exchange amplitude, it was shown that the Δ^+/Δ^- comparison is very insensitive to the relative amounts of the two. The data could be consistent with a significant contribution from $I=\frac{3}{2}$ exchange. Complementary evidence is provided by the Δ^-(1232) decay angular distribution, where the exchange of a $J=\frac{3}{2}$ baryon is required to provide the large amount of helicity-$\frac{3}{2}$ state present in the data. We conclude that both nucleon and Δ exchange are required for an adequate interpretation of $\Delta^-(1232)$ production in this experiment.

The cross section for backward ρ^0 production was compared with that for the backward reaction $\pi^- p \to p\rho^-$ and indicates that $I=\frac{1}{2}$ and $I=\frac{3}{2}$ exchanges contribute with comparable strengths. In order to fit the decay angular distribution of the ρ^0 it was necessary to introduce an interference with an s-wave $\pi^+\pi^-$ background. The amount of such background is not uniquely determined, but is consistent with the amount of background required for a fit to the $\pi^+\pi^-$ mass distribution in the ρ^0 region. It is tempting to associate the s-wave background with the excess of low-mass events seen in the $\pi^+\pi^-$ mass distribution but limited statistics preclude a definite conclusion. Nor can we draw any conclusions about the shape of the s-wave background or its possible resonant behavior.

The isotopic spin of the f^0 requires that it be produced by $I=\frac{1}{2}$ baryon exchange and its decay was consistent with that baryon having $J=\frac{1}{2}$. The differential cross section was not consistent with a simple exponential in u', evidencing a dip near

TABLE IV. Summary of factors used to obtain the cross-section normalization.

Quantity	Value
ρ (g/cm^3)	$0.073\pm(1.0\%)$
l (cm)	$30.5\pm(1.0\%)$
λ (cm)	$814.2\pm(1.2\%)$
E_1	$0.955\pm(0.5\%)$
E_2	$0.38\pm(13.3\%)$
W_1	$1.051\pm(1.6\%)$
W_2	$1.25\pm(2.0\%)$
N_s^c for sample	$12212\pm(2.5\%)$
N_m for sample	7578
F for sample	$5452\pm(1.7\%)$
N_t for sample	47095
σ_b for sample (nb/event)	$17.54\pm(13.9\%)$
σ_b for entire data sample (nb/event)	2.39 ± 0.33

$u' = 0.1$ (GeV/c)^2 [$u \sim -0.14$ (GeV/c)^2] and reinforcing the hypothesis of nucleon exchange.

ACKNOWLEDGMENTS

The successful completion of this experiment represents the combined efforts of many individuals. We thank the Accelerator Research Facilities Division of Argonne National Laboratory, especially the streamer-chamber crew, and the Argonne engineering staff, in particular J. Dawson, T. Kovarik, and J. Terandy. Dr. M. Buttram, Dr. T. O'Halloran, and Dr. P. Sokolsky made significant contributions in the early stages of the experiment. We are grateful for the labors of the scanning and measuring staff at the University of Illinois, the engineers who supported DOLLY, and the computer staff who provided assistance at all levels of the measuring and analysis. This research was supported in part by the Department of Energy and the National Science Foundation.

APPENDIX A: CORRECTIONS FOR EXPERIMENTAL ACCEPTANCE

To correct for the detection efficiency of the apparatus, a weight was calculated for each event that fit $n\pi^+\pi^-$. Monte Carlo techniques were used to generate many events physically equivalent to the observed event but differing in the direction of the incident beam, location of the primary vertex in the LH_2 target, and orientation about the beam direction. The weight for the observed event was then calculated from the probability of detecting the generated events.

Charged tracks were extrapolated to the walls of the streamer chamber to determine whether they caused a flare or if sufficient track length appeared outside the target vacuum box. It was also determined whether or not the extrapolated track traversed any counters used in anticoincidence in the trigger. The specific procedures followed may be found in Ref. 6 and are similar to those described in Ref. 1.

The probability of detecting the neutron depended on its entering the neutron spark chambers, interacting therein, and producing charged secondaries that triggered at least two of the three planes of scintillator.

Data taken on the reaction $pp \to nX^{++}$, a copious source of fast forward neutrons, were used to construct a map of the relative probability that an interacting neutron would satisfy the two out of three trigger requirement as a function of the transverse position of its interaction point in the spark chambers. The probability of detecting a neutron in a generated event was then found from the map with the assignment of 100% efficiency to neutrons incident along the central axis of the chambers.

The on-axis neutron detection efficiency, denoted by E_2 in Appendix B, was calculated from a Monte Carlo simulation of the response of the chambers and counters to incident neutrons with momenta between 2 and 8 GeV/c. This simulation incorporated models of Jones[12] and Barroncelli[13] for the description of the neutron and subsequent secondary interactions. Our conclusions were relatively insensitive to the choice of distributions from one or the other model and to reasonable variations of the parameters of either. The result, $E_2 = 0.38 \pm 0.05$, was included as a factor in the overall cross-section normalization described in Appendix B rather than in the weights of individual events. The value of E_2 is almost independent of neutron momentum. The quoted error reflects its sensitivity to reasonable variations in the input parameters.

In order to check the Monte Carlo simulation, a sample of measured pp events was fitted to the reaction $pp \to np\pi^+$. Events whose final state was $n\Delta^{++}$ were compared to bubble chamber data on $pp \to n\Delta^{++}$ at 8.1 GeV/c.[14] In particular, the cross section for this final state, calculated with the value for E_2 above, agreed within errors with the published cross section. The Monte Carlo simulation was also used to generate an efficiency map for the neutron chambers. This map was in good agreement with the empirical map described above and provided another check on the validity of the simulation.

APPENDIX B: CROSS-SECTION NORMALIZATION

The cross section for a particular process observed in this experiment may be expressed as

$$\sigma = \sigma_b N$$

where N is the number of events of a given kind. To obtain N, the number of observed events is corrected for experimental acceptance as well as for the effects of cuts made in selecting the sample. The cross-section basis, σ_b, in nb/event, may be expressed as

$$\sigma_b = \frac{N_s^c W_1 W_2}{n N_m E_1 E_2},$$

where N_s^c = the number of scanned two-prong events corrected for scanning accuracy and losses, N_m = the number of measured two-prong events, E_1 = the fraction of the streamer-chamber film that was scannable, E_2 = the probability that an on-axis neutron will interact in the spark chambers with secondaries satisfying the two-out-of-three logic, W_1 = a correction factor for events lost due to the

scattering of their secondaries in the LH_2 target, W_2 = a correction factor for neutrons interacting in the γ filter, and n is the nb equivalent. The nb equivalent, in events/nb, was calculated from

$$n = \frac{A_0}{M_H} \rho L \times 10^{-33},$$

where A_0 = Avogardro's number, M_H = the atomic weight of hydrogen, and ρ = the hydrogen density (g/cm^3). The total path length of beam particles in the liquid-hydrogen flask was obtained using

$$L = \lambda N_t F [1 - \exp(-l/\lambda)],$$

where l = the average length of liquid hydrogen traversed by a noninteracting beam particle (cm), N_t = the number of triggers in the data sample, F = the average beam flux recorded by counter B_4 per streamer chamber trigger, corrected for muon contamination in the beam (~6%) and for interactions upstream of the target, and λ = the attenuation length for the interaction or decay of 8 GeV/c π's in the target.

The cross-section basis was determined using about 10% of the data and was scaled to the total event sample. The factors which entered the determination of σ_b are listed in Table IV. We find $\sigma_b = 2.39 \pm 0.33$ nb/event, the error being dominated by the uncertainty in E_2.

The value of σ_b was checked in a study of 8 000 events for which the trigger simply required an interaction in the target. A scan was made for two- and four-prong interactions in the streamer chamber, and two-prong events were measured and fitted to $\pi^- p \to \pi^- p$. Our results on the $\pi^- p$ elastic and two- and four-prong topological cross sections were consistent with values measured elsewhere.[15]

---

*Deceased.

†Present address: University of Chicago, Chicago, Illinois.

‡Present address: E-Systems, Inc., Dallas, Texas.

§Present address: Argonne National Laboratory, Argonne, Illinois.

¶On leave at: National Science Foundation, Washington, D. C.

||Present address: Brookhaven National Laboratory, Upton, L. I., New York.

[1]A. Abashian *et al.*, Phys. Rev. D 13, 5 (1976).

[2]P. Benkheiri *et al.*, Phys. Lett. 68B, 483 (1977); A. Rougé *et al.*, *ibid.* 69B, 115 (1977).

[3]J. M. Watson *et al.*, Nucl. Instrum. Methods 105, 33 (1972).

[4]A. Abashian *et al.*, Nucl. Instrum. Methods 115, 445 (1974).

[5]For a description of the first run, see W. Mollet, Ph.D. thesis, University of Illinois, 1976 (unpublished). We note with great sadness the death of Bill Mollet in a climbing accident in August 1977.

[6]R. Wagner, Ph.D. thesis, University of Illinois, 1977 (unpublished).

[7]R. M. Brown and R. W. Downing, in *Proceedings of the International Conference on Advanced Data Processing for Bubble and Spark Chambers, Argonne National Laboratory, 1968,* edited by R. J. Royston (Argonne National Laboratory, Argonne, Illinois, 1968).

[8]See, for example, J. D. Jackson, Rev. Mod. Phys. 37, 484 (1965).

[9]J. E. Rice *et al.*, Phys. Rev. Lett. 27, 687 (1971).

[10]V. D. Barger and D. B. Cline, *Phenomenological Theories of High Energy Scattering* (Benjamin, New York, 1969).

[11]E. W. Anderson *et al.*, Phys. Rev. Lett. 22, 102 (1969).

[12]W. V. Jones, Phys. Rev. 187, 1868 (1969).

[13]A. Baroncelli, Nucl. Instrum. Methods 118, 445 (1974).

[14]J. Ginestet *et al.*, Nucl. Phys. B13, 283 (1969).

[15]A. R. Dzierba *et al.*, Phys. Rev. D 2, 2544 (1970); for elastic see Ref. 11.

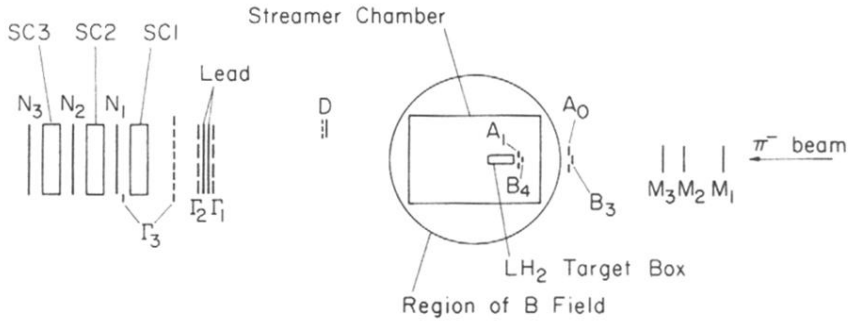

FIG. 1. Elevation view of experimental layout (not to scale). $M_{1,2,3}$ denote multiwire proportional chambers. $A_{0,1}$ and $B_{3,4}$ are scintillation counters. D, $\Gamma_{1,2,3}$, $N_{1,2,3}$ denote scintillation hodoscopes. $SC_{1,2,3}$ are spark chambers.

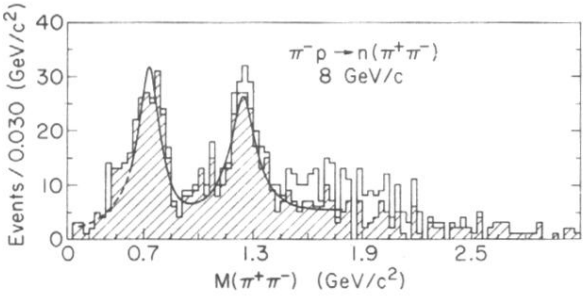

FIG. 10. The $\pi^+\pi^-$ invariant-mass distribution for 866 events. The shaded distribution results from the removal of 167 events with $M(p\pi^-) < 1.33$ GeV/c^2 and 9 events which were attributed to the final state $K^0_S\Lambda^0$. The solid curve is a fit of the data from 0.61 GeV/c^2 to 1.81 GeVc^2 to two Breit-Wigner distributions plus a smooth background.

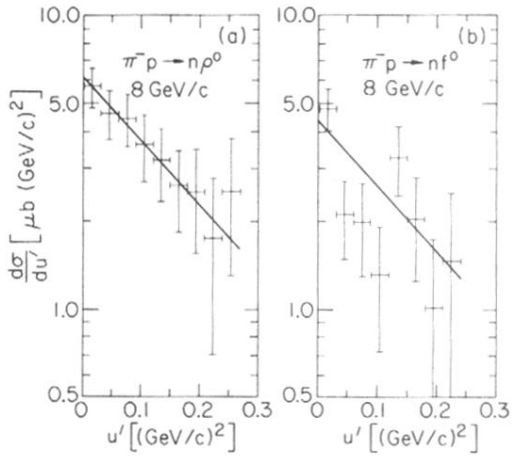

FIG. 11. The weighted distributions of u' to ρ^0 and f^0. A background subtraction, described in the text, has been performed in addition to the correction for experimental acceptance. The solid lines are the results of fits described in the text and whose parameters appear in Table II: (a) ρ^0 region (0.64–0.85 GeV/c^2), (b) f^0 region (1.15–1.33 GeV/c^2).

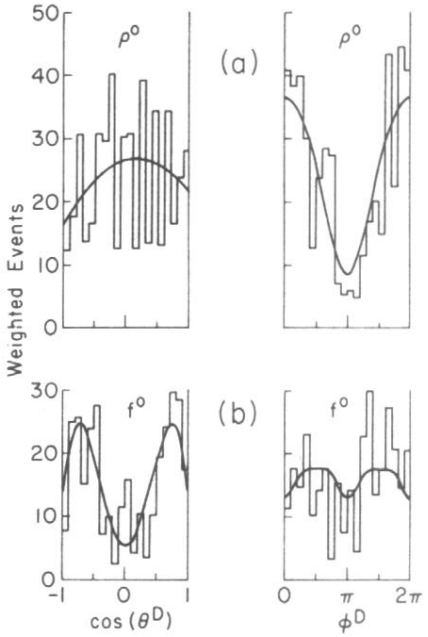

FIG. 12. The weighted decay angular distributions for ρ^0, (a), and f^0, (b), events. The solid curves display the distributions calculated from the density matrix elements given in Table III and the functional forms described in the text.

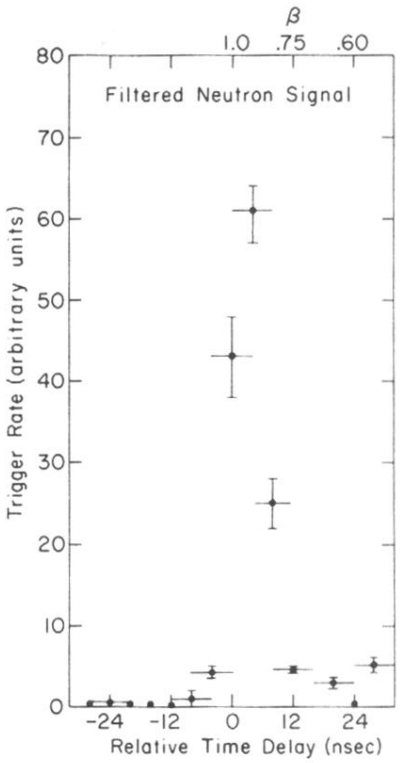

FIG. 2. The relative trigger rate vs the relative time delay between the filtered neutron signal and an 8-nsec-wide time gate. The origin is chosen so that zero delay corresponds to particles with $\beta = 1$. Counts at negative delay ($\beta > 1$) are due to accidental coincidences.

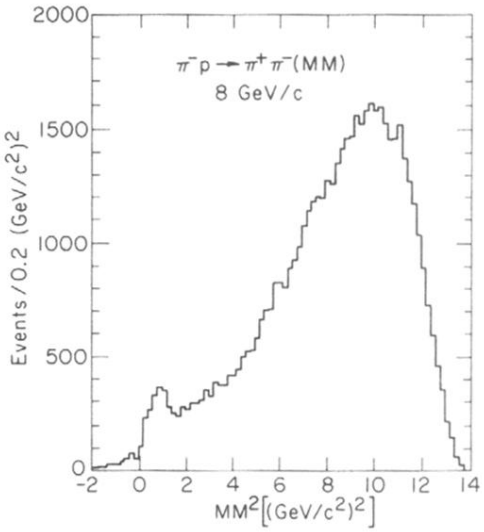

FIG. 3. The missing-mass-squared distribution for two-prong events successfully processed by VERTEX, calculated assuming that the outgoing charged particles are pions.

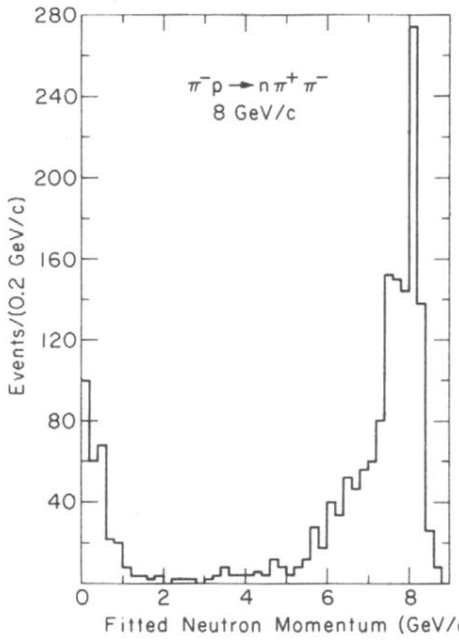

FIG. 4. The distribution of fitted neutron momentum for 1 663 events which fit $\pi^- p \rightarrow n \pi^+ \pi^-$.

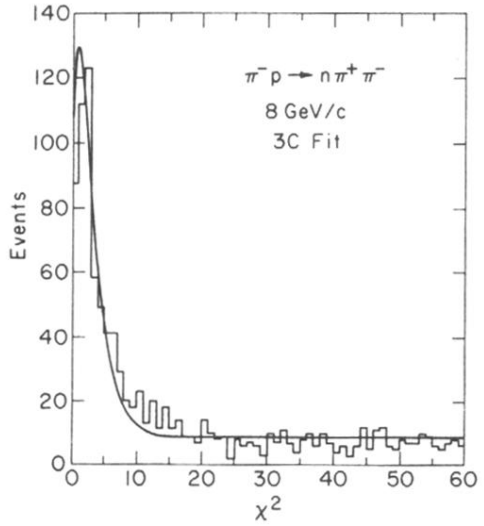

FIG. 5. The kinematic χ^2 distribution for 1 009 events satisfying the selection criteria described in the text. The solid curve is a fit to a constant plus a χ^2 distribution with three degrees of freedom.

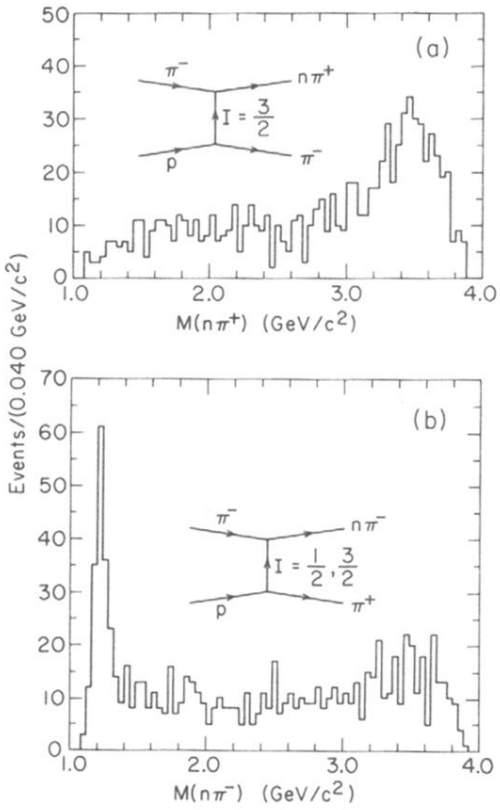

FIG. 6. The $n\pi$ invariant-mass distributions for the final sample of 866 events. The permitted isotopic-spin exchanges are also shown: (a) $M(n\pi^+)$, (b) $M(n\pi^-)$.

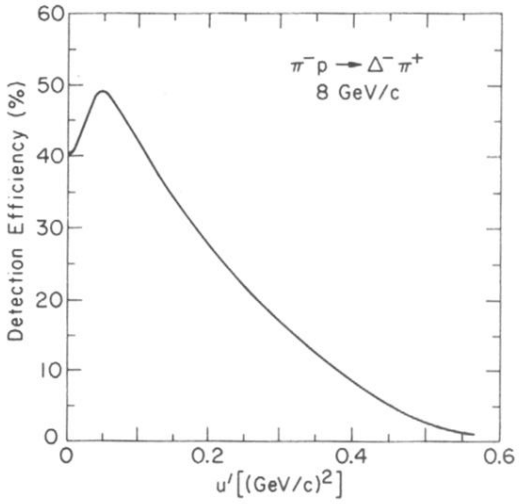

FIG. 7. The detection efficiency for events of the type $\pi^- p \rightarrow \Delta^-(1232)\pi^+$, calculated as a function of u' using the Monte Carlo described in the text. A value of $\rho_{11} = 0.18$ has been assumed.

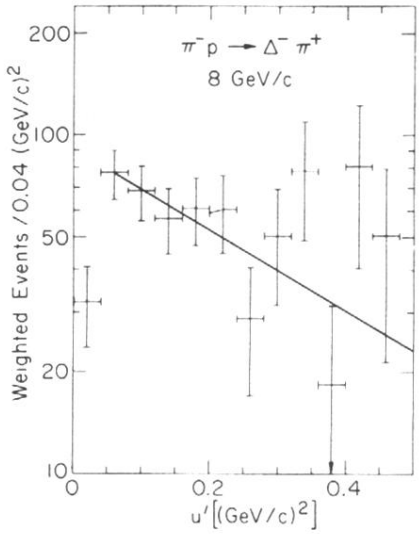

FIG. 8. The distribution of u' to the $\Delta^-(1232)$, corrected for the detection efficiency shown in Fig. 7. The solid line is the result of the fit described in the text and whose parameters appear in Table I.

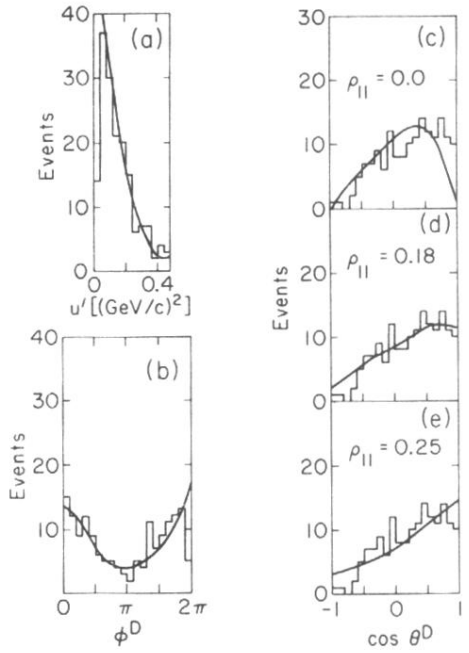

FIG. 9. The observed distributions of u', $\cos\theta^D$, and ϕ^D for the $\Delta^-(1232)$. The curves show the distributions for events generated by the Monte Carlo described in the text and subjected to the experimental acceptance. Except as noted, ρ_{11} was fixed at 0.18: (a) u', (b) ϕ^D, (c) $\cos\theta^D$ for $\rho_{11}=0.0$, (d) $\cos\theta^D$, (e) $\cos\theta^D$ for $\rho_{11}=0.25$.